Supplementary Material

A Structural Model of a P450-Ferredoxin Complex from Orientation-Selective Double Electron-Electron Resonance Spectroscopy

Alice M. Bowen,[1] Eachan O.D. Johnson,[2,†] Francesco Mercuri,[3] Nicola J. Hoskins,[2] Ruihong Qiao,[4] James S.O. McCullagh,[5] Janet E. Lovett,[1,^] Stephen G. Bell,[2,#] Weihong Zhou,[4,*] Christiane R. Timmel,[1,*] Luet Lok Wong,[2,*] and Jeffrey R. Harmer[1,§,*]

[1] Centre for Applied Electron Spin Resonance, Department of Chemistry, University of Oxford, Inorganic Chemistry Laboratory, South Parks Road, Oxford OX1 3QR, UK.
[2] Department of Chemistry, University of Oxford, Inorganic Chemistry Laboratory, South Parks Road, Oxford OX1 3QR, UK.
[3] Consiglio Nazionale delle Ricerche (CNR), Istituto per lo Studio dei Materiali Nanostrutturati (ISMN) Via P. Gobetti 101, 40129, Bologna, Italy.
[4] College of Life Sciences, Nankai University, Tianjin 300071, China.
[5] Department of Chemistry, University of Oxford, Chemistry Research Laboratory, Mansfield Road, Oxford OX1 3TA, UK.

[†] Current address: Broad Institute of MIT and Harvard, 415 Main St, Cambridge, MA 02142, USA.
[#] Current address: Department of Chemistry, University of Adelaide, Adelaide, SA 5005, Australia.
[§] Current address: Centre for Advanced Imaging, University of Queensland, St Lucia, QLD 4072, Australia.
[^] Current address: SUPA, School of Physics & Astronomy, University of St Andrews, North Haugh, St Andrews, KY16 9SS, UK.

Professor W. Zhou, E-mail: zhouwh@nankai.edu.cn
Professor C. R. Timmel, E-mail: christiane.timmel@chem.ox.ac.uk
Professor L. L. Wong, E-mail: luet.wong@chem.ox.ac.uk
Professor J. R. Harmer, E-mail: jeffrey.harmer@cai.uq.edu.au

S1 General

All chemicals, buffers, and reagents were of analytical grade or higher purity and were from Sigma-Aldrich or ThermoFisher Scientific, UK, and used without further purification. Media components were from Melford Laboratory, UK. *N*,*O*-*Bis*(trimethylsilyl)trifluoroacetamide with trimethylchlorosilane (BSTFA + TMCS, 99:1) was from Sigma. General DNA and microbiology experiments were carried out by standard methods. Enzymes for molecular biology were from ThermoFisher Scientific, Merck Bioscience or Invitrogen, UK. UV/Vis spectra and spectroscopic activity assays were performed at 30 ± 0.5 °C on an Agilent CARY-50 spectrophotometer. Gas chromatography (GC) analyses were performed on a ThermoFinnigan TRACE gas chromatograph equipped with a flame-ionization detector operating at 250 °C and a fused silica DB-1 column (30 m × 0.25 mm i.d. × 0.25 μm film thickness) using helium as carrier gas.

S2 Mutagenesis, protein production, purification and activity assays

The *RPA1871* gene encoding CYP199A2 from *Rhodopseudomonas palustris* CGA009, and the *RPB3614* gene from the *R. palustris* HaA2 strain that encoded HaPux had been cloned into T7-based pET expression vectors as described previously.[1,2] Site-directed mutagenesis was carried out using the QuikChange kit from Stratagene with oligonucleotides from Eurofin MWG Operon, Germany. Mutations were confirmed by automated DNA sequencing by the sequencing service at the Department of Biochemistry, University of Oxford.

Production and purification of the enzymes was carried out as described previously.[1-5] Briefly, after transformation of *E. coli* BL21 (DE3) with plasmid DNA harboring the desired gene, isolated colonies were used to inoculate 500 ml 2YT medium, which was incubated at 37 °C, 120 rpm until OD_{600} reached 0.8–1. The temperature of the incubator was lowered to 20 °C and recombinant protein production was induced with 40 μM IPTG. After incubation for a further 48 h, cells were harvested, resuspended in 50 mM Tris pH 7.4, 1 mM dithiothreitol (buffer T), and lysed by sonication at 4 °C. Cell debris was removed by centrifugation at 27000 *g* for 30 min at 4 °C. The desired protein in the supernantant was purified by anion exchange chromatography, firstly with a 200 mm × 50 mm DEAE Sepharose Fastflow (GE Healthcare) column, eluting with a linear gradient of 0–150 mM KCl (CYP199A2) or 100–400 mM KCl (HaPux) in buffer T. After desalting on a Sephadex

G-25 (GE Healthcare) column, final purification used a 120 × 26 mm Source 15Q (GE Healthcare) column, eluting with a linear gradient of 20–50 mM KCl (CYP199A2) or 60–240 mM (HaPux) in buffer T. Fractions containing the protein were pooled and concentrated to *ca.* 100 μM and then stored in 50% *v*/*v* glycerol at –20 °C. The CYP199A2 concentration was determined from the CO-difference spectrum with $\varepsilon_{450–490\ nm}$ = 91 mM^{-1} cm^{-1}.[6] HaPux concentrations were calculated using $\varepsilon_{416\ nm}$ = 11.6 mM^{-1} cm^{-1}.[2]

NADH turnover activity assays of the CYP199A2 mutants were performed with mixtures (total volume 1.2 ml) containing 50 mM Tris, pH 7.4, 0.5 μM CYP199A2, 5 μM HaPux, 0.5 μM PuR and 100 μg/mL bovine liver catalase.[2] The mixtures were equilibrated at 30 °C for 2 min. 4-Methoxybenzoic acid was added as a 100 mM stock solution in ethanol to a final concentration of 1 mM. NADH was added to *ca*. 320 μM (A_{340} = 2.00); the absorbance at 340 nm was monitored and the NADH turnover rate calculated using ε_{340} = 6.22 $mM^{-1}cm^{-1}$.

A 990 μl aliquot of the reaction mixture was mixed with 10 μl of a 25 mM solution of 9-hydroxyfluorene internal standard in DMSO and 2 μl of concentrated HCl was added.[1,2] The mixture was extracted three times with 0.4 ml of ethylacetate and the combined organic extracts were dried over $MgSO_4$. Solvent was evaporated under a stream of nitrogen and the residue was dissolved in 200 μl CH_3CN. Excess (25 μl) BSTFA + TMCS (99:1) was added and the mixture left at 50 °C for at least 2 h before GC analysis. The GC oven temperature was held at 100 ºC for 1 min and then increased at 15 ºC/min up to 220 ºC. The retention times for the trimethylsilyl esters were 4.30 min for 4-methoxybenzoic acid and 5.09 min for 4-hydroxybenzoic acid while the internal standard (9-hydroxyfluorene) eluted at 6.26 min. The results showed that all the surface cysteine mutants had the same selectivity as the wild type, giving 4-hydroxybenzoic acid as the only product.

S3 Spin labeling of CYP199A2

A 1 ml solution of *ca.* 10 μM wild-type or mutant CYP199A2 enzyme was buffer exchanged into phosphate buffered saline (PBS, ThermoFisher Scientific, UK) by repeated ultrafiltration-dilution cycles at 4 °C. The solution, with a final volume of 1 ml, was allowed to reach room temperature before 1% *v*/*v* DMSO was added, followed by a 10-fold molar excess of (1-oxyl-2,2,5,5-tetramethyl-Δ3-pyrroline-3-methyl)methane-thiosulfonate (MTSSL) (Toronto Research Chemicals, Canada) dissolved at 10 mM in DMSO. After incubation at 4 °C in the dark for 2 h the mixture was buffer exchanged as above into 10 mM

potassium phosphate buffer pH 7.4, resulting in concomitant removal of unreacted MTSSL. ES-MS analysis showed that the reaction proceeded with >95% labeling efficiency with wild type (Fig. S1) and the four mutants C226S/T42C, C226S/T315C, C226S/T345C, C226S/S404C.

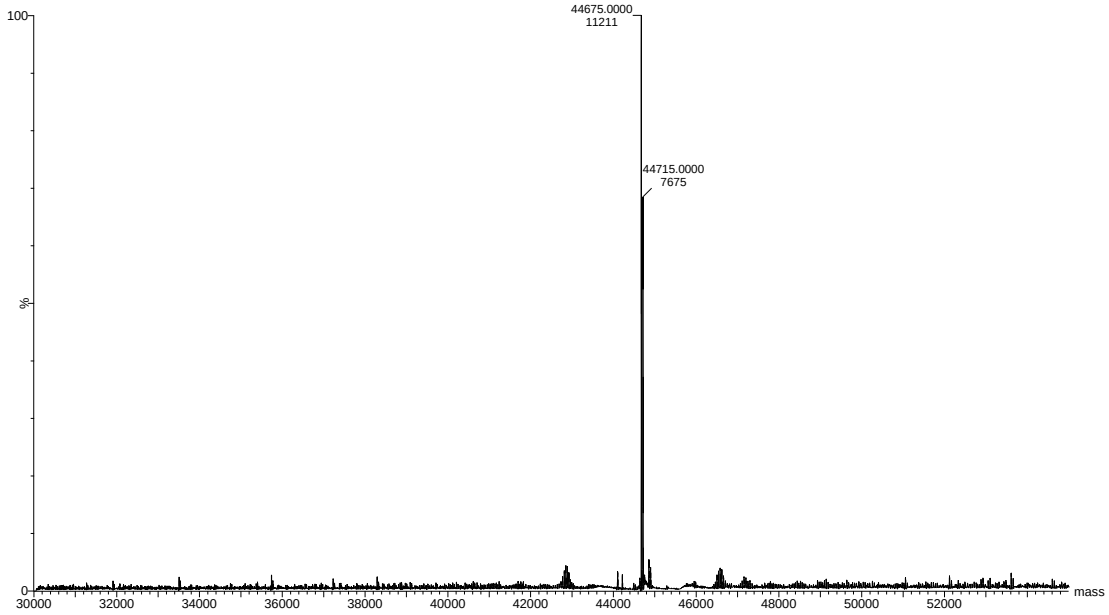

Fig. S1. The electrospray mass spectrum of WT CYP199A2 labeled with MTSSL showing the increase in RMM by 184 Da from 44491 Da for the unlabeled enzyme to 44675 Da from attachment of a single MTSSL.

S4 Sample preparation for orientation-selective DEER measurements

For each DEER spectra sample approximately 200 nmol CYP199A2 (wild-type or mutant) was spin-labeled at *ca*. 10 μM concentration, as described above. The spin-labeled enzyme was then buffer exchanged into 10 mM potassium phosphate pH 7.4, 1 mM 4-methoxybenzoic acid, in deuterium oxide and concentrated to >2 mM concentration. Approximately 200 nmol HaPux was buffer exchanged into the same buffer and concentrated to >2 mM. This was then mixed in an equimolar ratio with the spin-labeled CYP199A2 to form a >1 mM mixture of HaPux and spin-labeled CYP199A2 in a 15 ml centrifuge tube. A catalytic amount (0.01 eq.) of the ferredoxin reductase HaPuR was added and the centrifuge tube was closed with a SubaSeal before being flushed with CO and allowed to equilibrate for 30 min. Flushing was repeated and the sealed tube was then moved to a glove box (Belle Technology, UK). Glycerol-d^8 was added to 30% *v*/*v* followed by 1.5 equivalents of NADH

from a 20 mM stock in deuterium oxide. The HaPuR catalyzed the reduction of HaPux by NADH, and HaPux in turn reduced the 4-methoxybenzoic acid bound CYP199A2 to generate the ferrous heme that was rapidly trapped by CO to give the diamagnetic $Fe^{II}(CO)$ species. Once all of the CYP199A2 was reduced the excess NADH ensured that the HaPux was in its reduced, paramagnetic Fe^{3+}/Fe^{2+} state. Hence the spin-labeled CYP199A2 would be in complex with the HaPux and the DEER effect was detected between the nitroxide spin label on CYP199A2 and the Fe^{3+}/Fe^{2+} cluster of HaPux. A syringe fitted with a long needle was used to transfer the mixture from the centrifuge tube to a 3 mm diameter quartz tube for pulse EPR. The sample was then flash-frozen in liquid nitrogen and stored in a liquid nitrogen dewar.

S5 Sample preparation for orientation-independent DEER measurements

Control experiments showed that the Fe-S cluster of HaPux could be lost upon extended treatment with MTSSL as the cysteine thiolate ligands to the iron centres and the inorganic sulfide of the cluster could react with MTSSL. Although these side reactions could be controlled by varying the HaPux:MTSSL stoichiometry, the incubation time and temperature, some Fe-S cluster loss was observed from the UV/Vis spectrum of reaction mixtures. Fe-S cluster loss was further mitigated by labelling wild-type CYP199A2 at the C226 side chain, then forming the complex between HaPux-E54C and spin-labeled CYP199A2 in solution and then treating the complex with 2 equivalents of MTSSL for a shorter time. The expectation was that the Fe-S cluster was buried in the interface between the two proteins in the complex and would be protected from attack by MTSSL.

Approximately 200 nmol of wild-type CYP199A2 was treated with MTSSL, buffer exchanged into PBS, 1 mM 4-methoxybenzoic acid and concentrated to *ca.* 1 mM and then mixed to equimolarity with HaPux-E54C which had also been concentrated to *ca.* 1 mM in the same PBS, 1 mM 4-methoxybenzoic acid buffer. The ferredoxin-cytochrome mixture was then diluted with PBS, 1 mM 4-methoxybenzoic acid, to *ca.* 10 μM and allowed to reach room temperature, before adding 1% *v*/*v* DMSO followed by a two-fold molar excess of MTSSL dissolved at 0.01 g ml^{-1} in DMSO. The mixture was incubated at 4 °C for 2 hours before unreacted MTSSL was removed by buffer exchange into 10 mM potassium phosphate buffer pH 7.4, 1 mM 4-methoxybenzoic acid in deuterium oxide, and the sample was concentrated to 1 mM. HaPuR (0.01 eq.) was added and the 15 ml centrifuge tube was closed

with a SubaSeal before being flushed with CO gas and being allowed to equilibrate. Flushing was repeated and the mixture transferred on ice into a Belle Technology glove box. Glycerol-d^8 was added to 30% *v*/*v* followed by 0.5 eq. of NADH from a 25 mM stock in deuterium oxide. The NADH:CYP199A2 ratio ensured that the HaPux was present in its diamagnetic oxidized form while the Fe^{II}(CO) CYP199A2 was also diamagnetic, thus enabling the DEER effect between the nitroxide spin labels on the two proteins to be determined without complications from rapid relaxation by the paramagnetic iron centres. After incubation for 10 min a syringe fitted with a long needle was used to transfer the mixture to a 3 mm diameter quartz tube for pulse EPR. The sample was then flash-frozen in liquid nitrogen and stored in a liquid nitrogen dewar.

S6 Crystal structure determination of HaPux

Gene cloning, protein production and purification

The gene encoding HaPux was cloned into the expression vector pET26b by the NdeI and HindIII restriction sites. The recombinant plasmid was transformed into *E. coli* BL21 (DE3) and the transformed bacteria cells were cultured in 2YT medium at 37 °C with 25 μg ml^{-1} kanamycin. When the OD_{600} of the culture reached 0.6–0.8, 0.15 mM IPTG was added in order to induce the production of the recombinant protein. After further growth for 24 h at 20 °C, cells were harvested by centrifugation, resuspended in buffer P (10 mM Tris pH 7.4, 10% *v*/*v* glycerol, 1 mM DTT) and lysed by sonication at 4 °C. The crude extracts were centrifuged at 27000 *g* for 45 min at 4 °C to remove the cell debris.

The supernatant containing the protein was injected onto a Fastflow Q-Sepharose column (GE Healthcare, USA) and eluted with a gradient of 0–1 M NaCl in Buffer P. The eluted HaPux at *ca*. 260 mM NaCl was collected, concentrated by ultrafiltration to 1 mL and then buffer-exchanged into buffer A (20 mM Tris pH 7.4, 1 mM DTT). The protein solution in buffer A was concentrated to 1 mL and injected onto a Hitrap Q column (GE Healthcare) and eluted with a gradient of 0 to 1 M NaCl in buffer A. The protein eluted at *ca*. 170 mM NaCl was collected and concentrated by ultrafiltration to 500 μl and then applied to a Superdex-75 gel filtration chromatography column (GE Healthcare) equilibrated with buffer A containing 0.15 M NaCl for further purification. The purity of the protein was checked by SDS-PAGE.

Crystallization

Purified HaPux was concentrated in buffer A (containing 0.15 M NaCl) to 50 mg ml^{-1}. The sitting-drop vapor-diffusion method was used with Hampton Research Crystal Screen kit I, II and Index (Hampton Research, USA) to screen for crystals at 16 °C in 48-well plates. Two drops (each 1 µl) of the protein solution, with 15 or 25 mg ml^{-1} of protein, were mixed with 1 µl of reservoir solution separately and equilibrated against 100 µl of reservoir. After about a week several tawny needle-like red crystals were obtained from Crystal Screen kit II condition No.25 (0.01 M cobalt chloride hexahydrate, 0.1 M MES monohydrate pH 6.5, 1.8 M ammonium sulfate) and Crystal Screen kit I condition No.33 (4.0 M sodium formate). These initial conditions were optimized by changing the concentration of precipitant and protein, the buffer pH value and temperature. The crystals were grown by vapour diffusion in hanging drops at 16 °C in 24-well plates and equilibrated against 300 µl reservoir solution. Thick, plate-like crystals with the best diffraction quality were obtained at the condition (0.01 M cobalt chloride hexahydrate, 0.1 M MES pH 6.0, 1.8 M ammonium sulfate) at a protein concentration of 15 mg ml^{-1}.

Crystallographic data collection and processing

The X-ray diffraction data were collected on a Rigaku MicroMax-007 rotating-anode X-ray generator operating at 40 kV and 30 mA. Crystals was flash-cooled at −173 °C in a nitrogen gas stream after being cryoprotected with 25% *v*/*v* glycerol in reservoir solution. The diffraction data were collected to 2.30 Å resolution. The intensity set was indexed, integrated and scaled with the HKL-2000 package.[7] The crystals belonged to space group $P2_12_12_1$, with unit-cell parameters, a = 31.0, b = 73.1, c = 78.8 Å. There are two molecules in each ASU. Complete data collection statistics are summarised in Table S1.

Structure determination and refinement

For the structure determination the molecular-replacement (MR) method Phaser in the CCP4 suite[8] was used to find the phases. The structure of putidaredoxin from *Pseudomonas putida* (PDB code: 1R7S)[9] was used as a search model. The model was rebuilt with Coot [10] and refined with REFMAC5.[11] The stereochemical quality of the refined structure was checked with the program MolProbity.[12] A summary of the structure refinement statistics is provided in Table S1. The coordinates have been deposited in the PDB with accession code 4LTU.

Table S1 Data collection and refinement statistics of HaPux from *Rhodopseudomonas palustris* HaA2

	HaPux
Data collection statistics	
Space group	$P2_12_12_1$
Cell dimensions *a*/*b*/*c* (Å)	31.0/73.1/78.8
Wavelength (Å)	1.5418
Resolution (Å)	50–2.30 (2.38–2.30)
Average $I/\sigma(I)$[1]	7.75 (2.47)
Completeness (%)[1]	98.4 (95.0)
Average Redundancy[1]	4.7 (4.1)
R_{merge} (%)[1,2]	14.1 (41.2)
Molecules in one ASU	2
Structure refinement statistics	
Resolution (Å)	53.62–2.30
Average *B*-factor (Å^2)	22.1
R_{work}/R_{free} (%)[3]	22.8/29.8
r.m.s.d. bond lengths (Å)	0.014
r.m.s.d. bond angles (°)	1.598
Ramachandran favoured (%)	96.15
Ramachandran outliers (%)	0.48
MolProbity score	1.70
Poor rotamers (%)	2.30
Clash scores, all atoms	3.77

[1] Values in parentheses correspond to the highest-resolution shell.

[2] $R_{merge} = \Sigma_h \Sigma_i |I_i - \langle I \rangle| / \Sigma_h \Sigma_i I_i$, where I_i is the **i**th intensity measurement of reflection h, and <I> is the average intensity from multiple observations [3] $R_{work}/R_{free} = \Sigma ||F_o| - |F_c|| / \Sigma |F_o|$, where F_o and F_c are the observed and calculated structure factors, respectively.

[3] $R_{work}/R_{free} = \Sigma ||F_o| - |F_c|| / \Sigma |F_o|$, where F_o and F_c are the observed and calculated structure factors, respectively.

S7 EPR experimental

Optimum DEER measurement temperature

An optimum DEER measurement temperature was sought which maximizes the T_2 relaxation time of the NO$^{\bullet}$ radical (detection spins) and the T_1 relaxation time of the $[Fe_2S_2]^{+\bullet}$ cluster (pump spins). T_M and T_1 were measured via a 2-pulse spin-echo and inversion recovery experiment, respectively, at several temperatures. NO$^{\bullet}$: T_2 ~ 2.25/2.25 µs and T_1 ~ 600/1000 µs at 50/20 K. $[Fe_2S_2]^{+\bullet}$: T_2 ~ 1.0/1.2 µs and T_1 ~ 125/2.5 µs at 50/20 K. DEER measurements require a species with a long T_2 time for the detection sequence and were applied to the NO$^{\bullet}$ radical at the position of its maximum echo intensity. Additionally, the T_1 of the $[Fe_2S_2]^{+\bullet}$ spins needs to be long compared to the DEER sequence length of ~4 µs, which requires a temperature around 20 K. Most experiments were carried out at this temperature, but as a consequence require a slow repetition rate (20 ms) so that the NO$^{\bullet}$ radical signal is not detrimentally saturated. The T_1 time of the NO$^{\bullet}$ radical is convenient for measurements at 50 K but under these conditions considerable relaxation of the $[Fe_2S_2]^{+\bullet}$ spin occurs which decreases dramatically the efficiency of the pump π pulse.

DEER measurement fields and positions

Echo-detected EPR spectra were recorded by integrating the echo intensity created with the mw pulse sequence $\pi/2$-τ-π-τ-*echo* with mw pulse lengths $t_{\pi/2}$ = 40 ns, t_{π} = 80 ns, and a τ = 500 ns.

S8 Pattern Search Algorithm

A schematic overview is shown below of the pattern search algorithm which optimized simultaneously the position (x, y, z) and rotation (α, β, γ) of CYP199A2 relative to HaPux to optimize the DEER trace simulations to experimental data.

1	Compute R^{tot} using an initial guess for the starting model parameters, **p** = ($x, y, z, \alpha, \beta, \gamma$).
2	Generate a grid or mesh of model parameter values around the current values, using the current mesh size dr and $d\xi$. **p** = ($x\pm dr, y\pm dr, z\pm dr, \alpha\pm d\xi, \beta\pm d\xi, \gamma\pm d\xi$).
3	Evaluate the objective function R (Eq. 3) for each of the $3^6 = 729$ points in the grid in the 6-dimensional parameter space. $R(x,y,z,\alpha,\beta,\gamma) = R_{42} + R_{226} + R_{315} + R_{345} + R_{404} + R_{226-54}$ Eq. 3b
4	If one of the 64 computed R values is lower than the current value, then the poll is successful. - the model parameters, **p** = ($x, y, z, \alpha, \beta, \gamma$), giving the R minimum become current. - the mesh size is doubled: $dr=2dr$ and $d\xi=2\,d\xi$. - the algorithm proceeds to Step 2.
	If the poll is unsuccessful - The mesh size is halved, $dr=dr/2$ and $d\xi=2\,d\xi$. - If the mesh size dr and $d\xi$ are below their thresholds, stop and exit Otherwise retain the current model parameters and proceeds to Step 2.

Table S2. Interfacial interactions after optimization in vacuum for the top 6 ranked DEER-docked structures for the CYP199A2-HaPux complex. Fe(1) –Fe distance is that between the iron atom Fe(1) of the [Fe_2S_2] cluster closest to the heme iron (Fe). Residue interactions in brackets are denoted as; HB: hydrogen bond, VDW: van der Waals/hydrophobic interaction, SB: salt bridge.

HaPux residue (locale)	**CYP199A2 residue**					
	Rank 1	**Rank 2**	**Rank 3**	**Rank 4**	**Rank 5**	**Rank 6**
Fe(1)-Fe distance	15.4 Å	15.6 Å	15.6 Å	16.0 Å	15.9 Å	15.8 Å
Fe(1)-Fe(1) distance *vs*. Rank 1	–	0.5 Å	0.6 Å	0.8 Å	1.0 Å	1.0 Å
Glu38 (Fe-S loop)	Gln364 (HB)	Gln364 (HB)	Gln364 (HB)	Gln364 (HB)	Gln364 (HB)	Gln364 (HB)
	Arg368 (SB)	Arg368 (SB)	Arg368 (SB)	Arg368 (SB)		
	Met360 (VDW)	Met360 (VDW)	Met360 (VDW)	Met360 (VDW)	Met360 (VDW)	Met360 (VDW)
					Arg111 (SB)	Arg111 (SB)
Cys39 (Fe-S loop)	Met360 (VDW)	Met360 (VDW)	Met360 (VDW)			
Asn42 (Fe-S loop)	Asn71 (HB)	Asn71 (VDW)	Asn71 (VDW)	Asn71 (HB)		
	Gly357 (VDW)	Gly357 (VDW)	Gly357 (VDW)	Gly357 (VDW)	Gly357 (VDW)	Gly357 (VDW)
	Val358 (VDW)	Val358 (VDW)	Val358 (VDW)	Val358 (VDW)	Val358 (VDW)	Val358 (VDW)
Val44 (Fe-S loop)	Arg111 (HB)	Arg111 (HB)	Arg111 (HB)	Arg111 (HB)	Arg111 (HB)	Arg111 (HB)
	Arg111 (VDW)	Arg111 (VDW)	Arg111 (VDW)	Arg111 (VDW)	Arg111 (VDW)	Arg111 (VDW)
	His107 (VDW)	His107 (VDW)	His107 (VDW)	His107 (VDW)	His107 (VDW)	His107 (VDW)
	Thr108 (VDW)	Thr108 (VDW)	Thr108 (VDW)		Thr108 (VDW)	Thr108 (VDW)
	Val358 (VDW)	Val358 (VDW)	Val358 (VDW)	Val358 (VDW)	Val358 (VDW)	Val358 (VDW)
Cys45 (Fe-S loop)	Arg111 (VDW)	Arg111 (VDW)	Arg111 (VDW)		Arg111 (VDW)	

Asn66 (α3 helix)	Thr108 (VDW)	Thr108 (VDW)	Thr108 (VDW)	Thr108 (VDW)	Thr108 (VDW)	Thr108 (VDW)
Asp69 (α3 helix)	Lys116 (SB) Lys116 (HB)	Lys116 (SB) Lys116 (HB)	Lys116 (SB)	Lys116 (SB)	Lys116 (SB) Lys116 (HB)	Lys116 (SB)
Leu70 (α3 helix)	Ser115 (VDW) Ala112 (VDW)	Ser115 (VDW) Ala112 (VDW)	Ser115 (VDW) Ala112 (VDW)	Ser115 (VDW) Ala112 (VDW)	Ser115 (VDW) Ala112 (VDW)	Ser115 (VDW) Ala112 (VDW)
Asp72 (α3 helix)				Lys116 (SB)		Lys116 (SB)
Gly73 (α3 helix)	Ser119 (VDW) Pro120 (VDW)	Ser119 (VDW) Pro120 (VDW)	Ser119 (VDW) Pro120 (VDW)	Ser119 (VDW) Pro120 (VDW)	Ser119 (VDW) Pro120 (VDW) Ala121 (VDW)	Ser119 (VDW) Pro120 (VDW)
Thr74 (α3 helix)	Pro120 (VDW) Ala121 (HB, VDW)	Pro120 (VDW) Ala121 (HB, VDW)	Pro120 (VDW) Ala121 (HB, VDW)		Pro120 (VDW) Ala121 (VDW)	Pro120 (VDW) Ala121 (HB)
Ala75 (α3 helix)	Lys124 (HB) Pro120 (VDW)	Lys124 (HB) Pro120 (VDW)	Lys124 (HB) Pro120 (VDW)		Pro120 (VDW)	Pro120 (VDW)
Thr106 (C-terminus)	Lys124 (SB) Arg285 (VDW) Pro120 (VDW)	Lys124 (SB) Arg285 (HB) Pro120 (VDW)	Lys124 (SB) Arg285 (HB) Pro120 (VDW)	Lys124 (SB) Pro120 (VDW)	Lys124 (SB) Pro120 (VDW)	Lys124 (SB) Arg285 (HB)

Table S3. Interfacial interactions after optimization in water for the top 6 ranked DEER-docked structures for the CYP199A2-HaPux complex. Fe(1)–Fe distance is that between the iron atom Fe(1) of the [Fe_2S_2] cluster closest to the heme iron (Fe). Residue interactions in brackets are denoted as; HB: hydrogen bond, VDW: van der Waals/hydrophobic interaction, SB: salt bridge.

HaPux residue (locale)	**CYP199A2 residue**					
	Rank 1	**Rank 2**	**Rank 3**	**Rank 4**	**Rank 5**	**Rank 6**
Fe(1)-Fe distance	15.4 Å	15.6 Å	15.5 Å	15.9 Å	15.7 Å	15.9 Å
Fe(1)-Fe(1) distance *vs*. Rank 1	–	0.4 Å	0.5 Å	0.7 Å	0.7 Å	0.7 Å
Glu38 (Fe-S loop)	Gln364 (HB) Arg368 (SB) Met360 (VDW)	Gln364 (HB) Arg368 (SB) Met360 (VDW)	Gln364 (HB) Arg368 (SB) Met360 (VDW)	Gln364 (HB) Arg368 (SB) Met360 (VDW)	Gln364 (HB) Arg368 (SB) Met360 (VDW)	Gln364 (HB) Met360 (VDW) Arg111 (SB)
Cys39 (Fe-S loop)	Met360 (VDW)	Met360 (VDW)	Met360 (VDW)		Met360 (VDW)	
Asn42 (Fe-S loop)	Asn71 (HB) Gly357 (VDW) Val358 (VDW)	Asn71 (VDW) Gly357 (VDW) Val358 (VDW)	Asn71 (VDW) Gly357 (VDW) Val358 (HB, VDW)	Asn71 (HB) Gly357 (VDW) Val358 (VDW)	 Gly357 (VDW) Val358 (VDW)	 Gly357 (VDW) Val358 (VDW)
Val44 (Fe-S loop)	Arg111 (HB) Arg111 (VDW) His107 (VDW) Thr108 (VDW) Val358 (VDW)	Arg111 (HB) Arg111 (VDW) His107 (VDW) Thr108 (VDW) Val358 (VDW)	Arg111 (HB) Arg111 (VDW) Thr108 (VDW) 	Arg111 (HB) Arg111 (VDW) His107 (VDW) Val358 (VDW)	Arg111 (HB) Arg111 (VDW) His107 (VDW) Thr108 (VDW) Val358 (VDW)	Arg111 (HB) Arg111 (VDW) His107 (VDW) Thr108 (VDW)

Cys45 (Fe-S loop)	Arg111 (VDW)	Arg111 (VDW)	Arg111 (VDW) Ser115 (HB)	Ser115 (HB)	Arg111 (VDW)	Arg111 (VDW)
Asn66 (α3 helix)	Thr108 (VDW)	Thr108 (VDW)	Thr108 (VDW)		Thr108 (VDW)	Thr108 (VDW)
Asp69 (α3 helix)	Lys116 (SB) Lys116 (HB)	Lys116 (SB) Lys116 (HB)	Lys116 (SB)	Lys116 (SB)	Lys116 (SB) Lys116 (HB)	Lys116 (SB)
Leu70 (α3 helix)	Ser115 (VDW) Ala112 (VDW)	Ser115 (VDW) Ala112 (VDW)	Ser115 (VDW) Ala112 (VDW)	Ser115 (VDW) Ala112 (VDW)	Ser115 (VDW) Ala112 (VDW)	Ser115 (VDW) Ala112 (VDW)
Asp72 (α3 helix)				Lys116 (SB)		Lys116 (SB)
Gly73 (α3 helix)	Ser119 (VDW) Pro120 (VDW)	Ser119 (VDW) Pro120 (VDW)	Ser119 (VDW) Pro120 (VDW)	Ser119 (VDW) Pro120 (VDW)	Ser119 (VDW) Pro120 (VDW) Ala121 (HB, VDW)	Ser119 (VDW) Pro120 (VDW)
Thr74 (α3 helix)	Pro120 (VDW) Ala121 (HB)	Pro120 (VDW) Ala121 (HB)	Pro120 (VDW) Ala121 (VDW)		Pro120 (VDW) Ala121 (VDW)	Pro120 (VDW) Ala121 (HB)
Ala75 (α3 helix)	Lys124 (HB) Pro120 (VDW)	Lys124 (HB) Pro120 (VDW)	Lys124 (HB)		Pro120 (VDW)	Pro120 (VDW)
Thr106 (C-terminus)	Lys124 (SB) Arg285 (VDW) Pro120 (VDW)	Lys124 (SB) Arg285 (VDW) Pro120 (VDW)	Lys124 (SB) Arg285 (HB) Pro120 (VDW)	Lys124 (SB) Pro120 (VDW)	Lys124 (SB, HB) Pro120 (VDW)	Lys124 (SB, HB) Arg285 (HB)

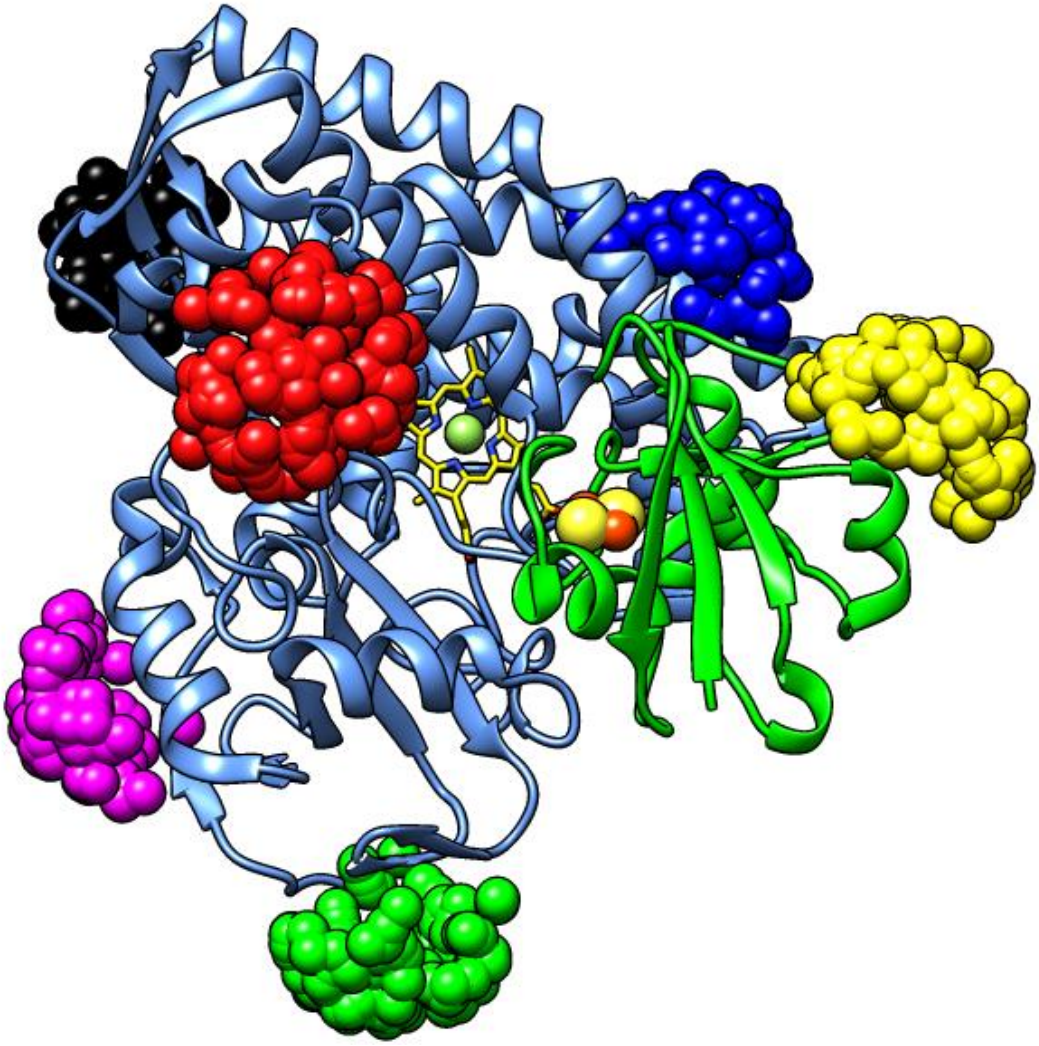

Fig. S2. Cartoon representation of the CYP199A2-HaPux complex showing the distribution of MTSSL spin labels. CYP199A2 is in blue and the nitrogen atoms of the MTSSL spin label rotamers are shown as spheres (Thr42 magenta, S226 dark blue, Thr315 green, Thr345 red, Ser404 black). HaPux is in green, the [Fe_2S_2] cluster is represented by the yellow and red spheres, and the nitrogen atoms of the MTSSL spin label rotamers as yellow spheres (D54).

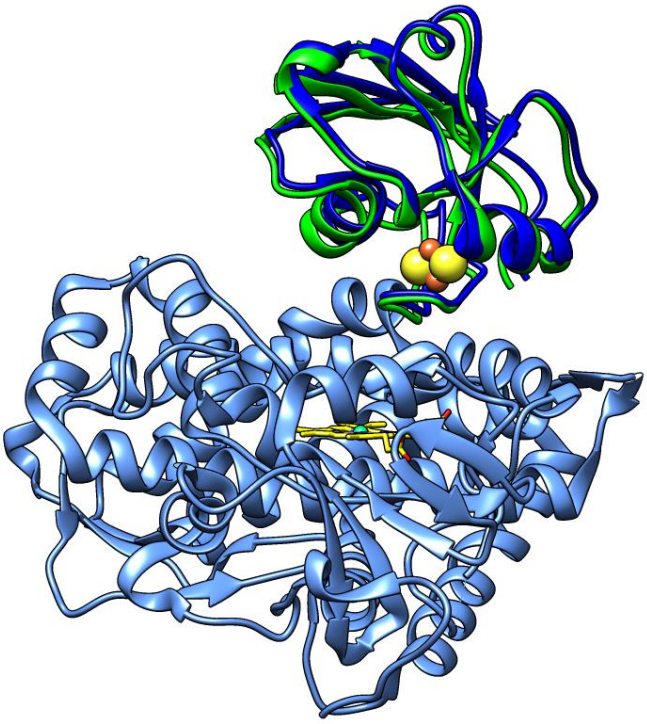

Fig. S3. A test of the docking software was undertaken by docking P450cam to Pdx and comparing the output strucutres with the complex determined by X-ray crystallography (PDB code: 5GXG).[13] PatchDock produced a P450cam-Pdx complex that is essentially identical to the one from crystallography with a root-mean-squared-deviation (RMSD) of 1.53 Å between all atoms. This value lies within the RMSD clustering parameter of 4 Å used in all PatchDock calculations. The X-ray structure of the complex is shown in blue (P450cam is pale blue and Pdx is dark blue) and the docked position of the Pdx with the smallest RMSD to the X-ray structure generated by PatchDock is shown in green. No pre-determined interface residues were defined to restrict this PatchDock calculation. However, if the Pdx interface was defined to be equivalent to that used for the HaPux, a very similar result was also obtained with an RMSD of 2.81 Å between all atoms of the crystal structure and the model generated, still within the PatchDock clustering parameter of 4 Å.

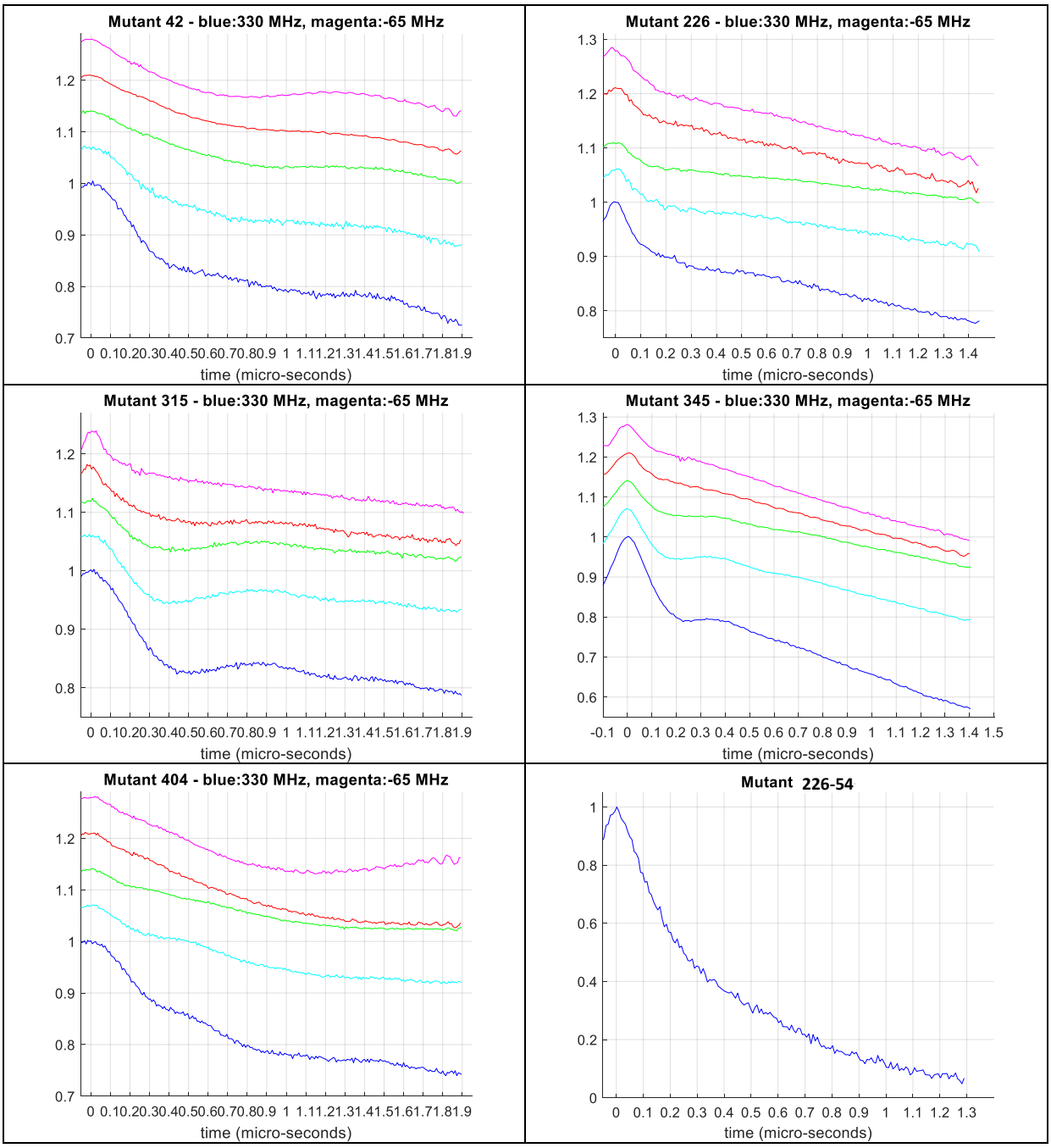

Fig. S4. X-band DEER traces from the six mutant samples. For the orientation-selective DEER the detection to pump frequency offsets are $\Delta\nu$ = −65, 80, 165, 247, 330 MHz. For mutant 226-54 (NO•-NO•), $\Delta\nu$ = 65 MHz. Inspection of the traces reveals that some of the DEER traces exhibit weak oscillations due to small couplings of magnetic nuclei to the paramagnetic center; see for example mutant 404, blue (bottom) trace, which has a persistent oscillation at approximately 1.2 MHz due to ^{14}N nuclei, the pink (top) trace exhibits weak oscillations due to ^{1}H nuclei.

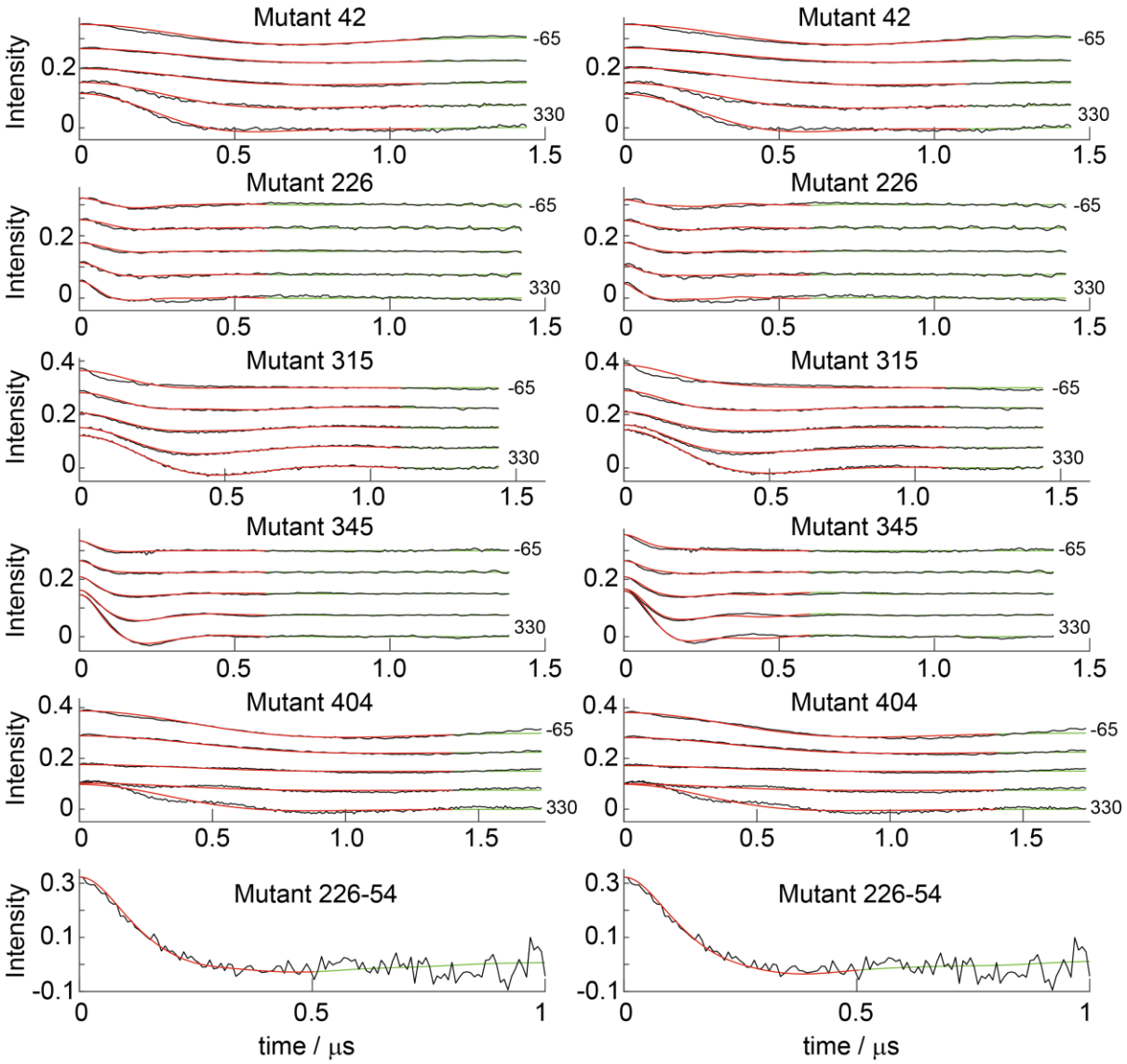

Fig. S5. X-band DEER traces from the six mutant samples. (Left) best fit to the DEER traces using rotamers calculated by mtsslWizard, DEER-fit complex with the lowest residual, R^{tot} = 0.034. (Right) best ranked PatchDock/FireDock structure using the rotamer library 175K_flat, DEER-docked complex with R^{tot} = 0.040. Experimental traces are in black, with simulations in red/green. The pump to detection frequency offsets Δν are −65, 80, 165, 247, 330 MHz, for mutant 226-54 ($NO^{\bullet}$-$NO^{\bullet}$) Δν = 65 MHz. All traces have had the background $B(t)$ and the un-modulated part (1-Δ) removed and then $\Delta f(t)$ is plotted (see Eq. 2). For each DEER trace the residual (Eq. 3b) is calculated from the red section only to weight the important first oscillations. Note that some DEER traces exhibit weak oscillations from ^{14}N and ^{1}H electron-nuclear interactions, see Figure S4 for further details.

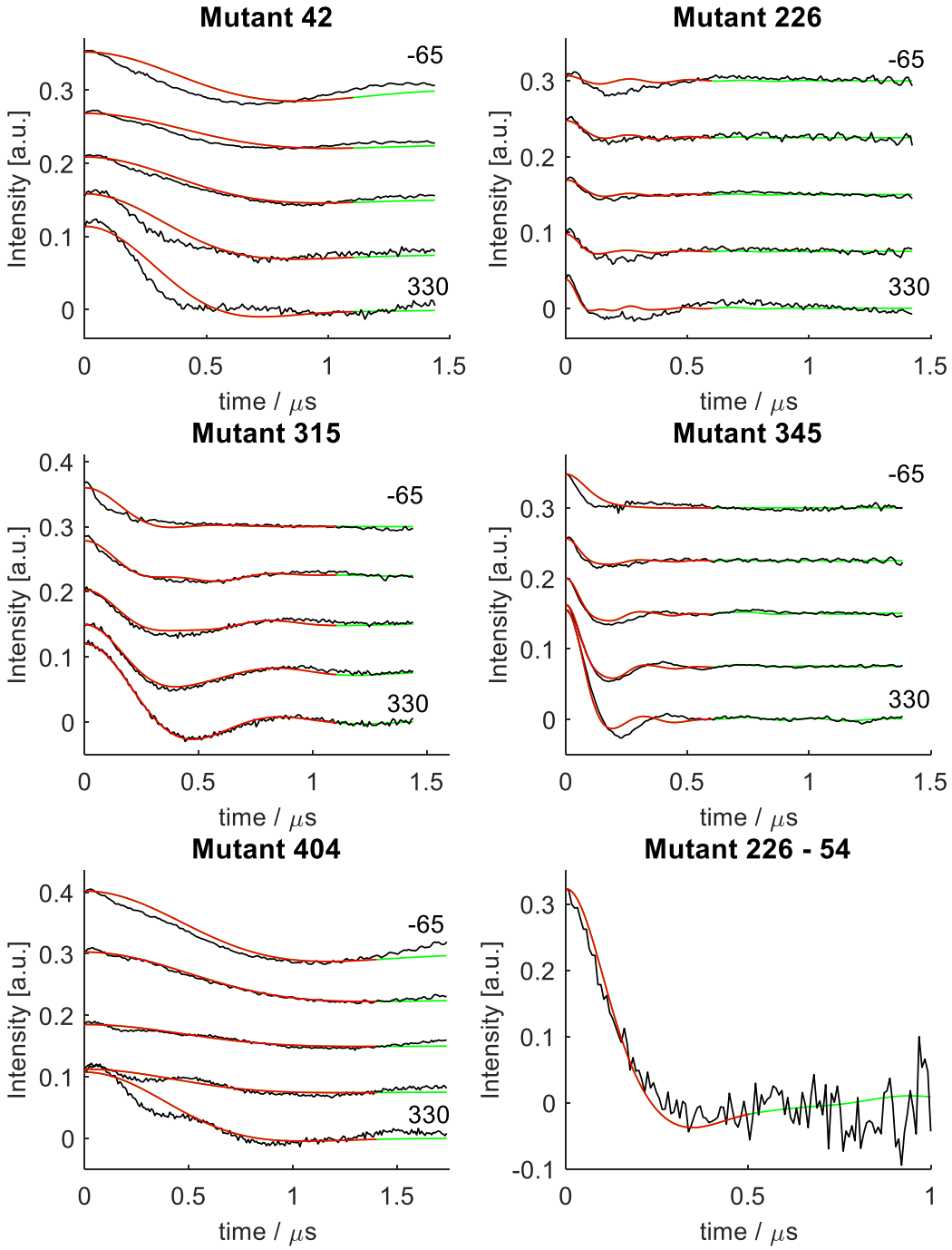

Fig. S6. X-band DEER traces from the six mutant samples and simulations for the optimized DEER-fit complex using the rotamer library 175K-UFF-216-CASD, $R^{tot} = 0.51$. This represents the worst fit to the DEER data from the 14 methods used to compute the rotamers as defined in Table 2. However, the resulting DEER-fit complex has a very similar relative orientation of CYP199A2 to HaPux as the best DEER-fit complex (Fig. 3 in the main text). This demonstrates that the complex defined by fitting to the DEER traces is not critically sensitive to variations in the rotamer distributions resulting from the different computation methods (rotamer libraries). Experimental traces are in black, with simulations in red/green. The pump to detection frequency offsets Δν are −65, 80, 165, 247, 330 MHz, for mutant 226-54 (NO•-NO•) Δν = 65 MHz. All traces have had the background $B(t)$ and the un-modulated part (1-Δ) removed and then $\Delta f(t)$ is plotted (see Eq. 2). Note that some DEER traces exhibit weak oscillations from ^{14}N and ^{1}H electron-nuclear interactions, see Figure S4 for further details.

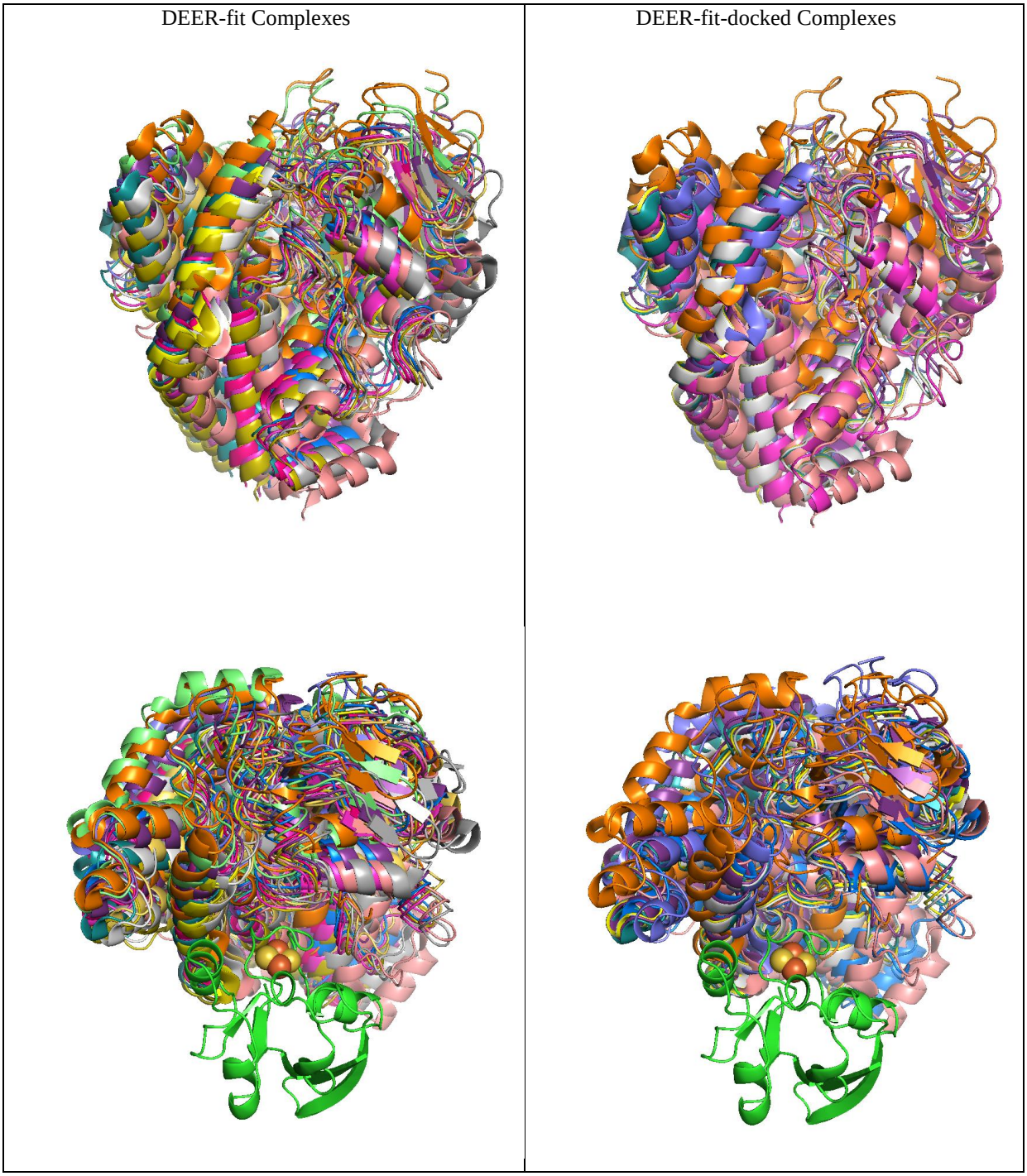

Fig. S7. Cartoon representation of the fourteen DEER-fit (left) and DEER-fit-docked (right) complexes. All CYP199A2-HaPux complexes have a common HaPux alignment, The two top figures have HaPux removed.

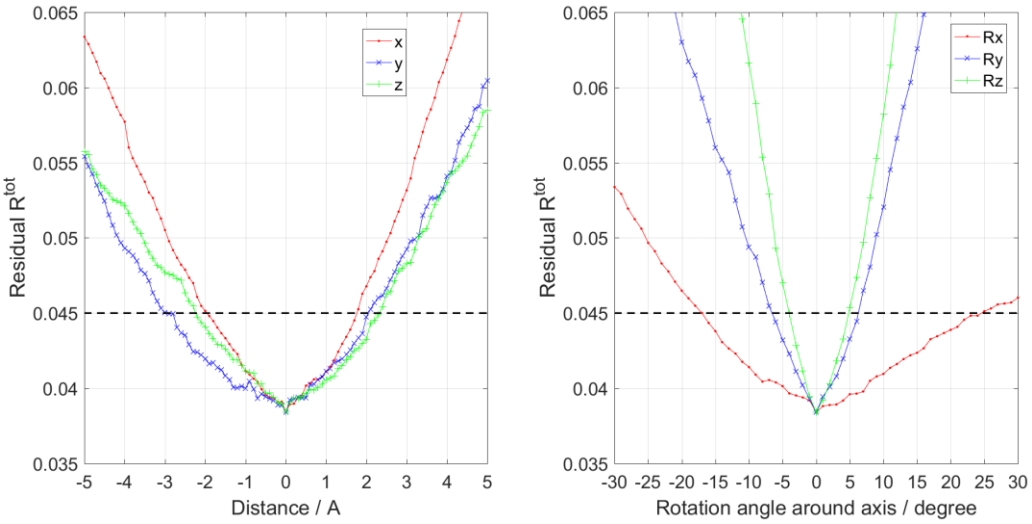

Fig. S8. Variation of $R^{tot}(x, y, z, \alpha, \beta, \gamma)$ around the global minimum which defines the best DEER-fit structure. Each curve was generated by varying one of the model parameters and keeping the others fixed. The rotations around the axes *x*, *y* and *z* are computed using $R_x(\pi/2,\beta, -\pi/2)$, $R_y(\alpha,0,0)$, and $R_z(0,\beta,0)$, respectively. The Euler angles (α,β,γ) are relative to rotation around the heme iron of CYP199A2. HaPux is fixed and defined by the coordinates in Table 1. The $R^{tot}_{cut\text{-}off} = 0.045$ is show as a solid black line. The best ranked DEER-docked structure generated from PatchDock/FireDock has an $R^{tot} = 0.0403$ that lies very close to the global minimum. The 6th best ranked DEER-docked structure has an $R^{tot} = 0.0445$.

The standard error in the fitted model parameters $\mathbf{p} = (x, y, z, \alpha, \beta, \gamma)$ can be estimated from the expression

$$\sigma_p = \sigma_r\sqrt{d_{ii}},$$

where

$$\sigma_r = \sqrt{R_{mutant}}$$

and R_{mutant} is the sum-of-the-squares of the residuals defined in Eq. 3. d_{ii} is the i^{th} diagonal element of the inverted curvature matrix $(\mathbf{J}^t\mathbf{J})^{-1}$, and

$$\mathbf{J} = \partial\mathbf{r}_i/\partial p_i$$

is the Jacobian matrix, the derivative of the residuals $\mathbf{r}_i$ with respect to the model parameters $\mathbf{p}_i$. Each column in **J** (six in total) was computed numerically according to

$$\frac{\partial\mathbf{r}_i}{\partial p_i} \cong \frac{\mathbf{r}(\mathbf{p}+\Delta p_i)-\mathbf{r}(\mathbf{p})}{\Delta p_i}.$$

The bold symbol represents a vector of residuals (**r**) or of the model parameters **p**. The computed standard error in the fitted model parameters are

$\sigma_x \cong \sigma_y \cong \sigma_z \sim 0.5$ Å, $\sigma_\alpha \sim 7°$, $\sigma_\beta \sim 3°$, $\sigma_\gamma \sim 2°$.

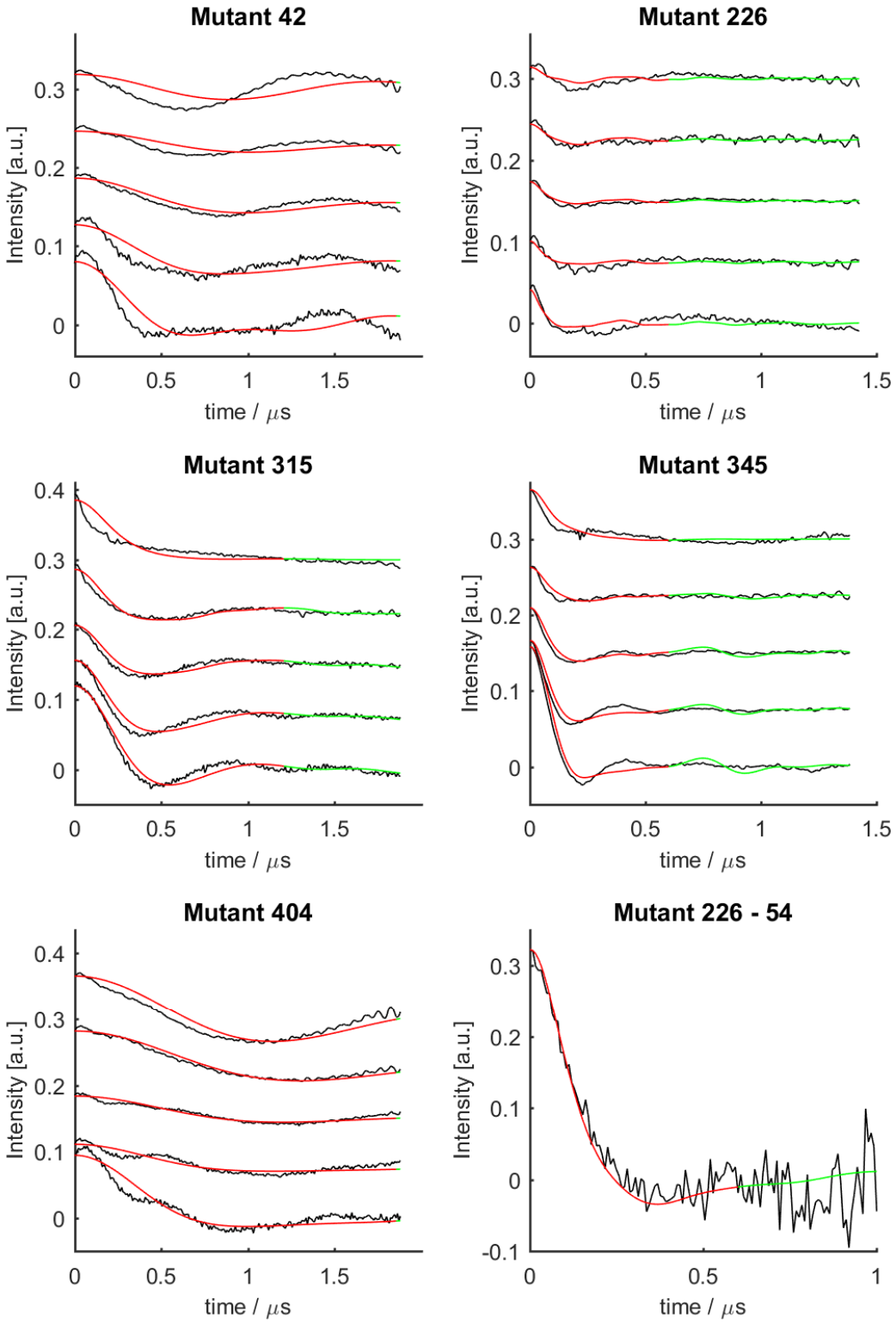

Fig. S9. X-band DEER traces from the six mutant samples and simulations for the **6th ranked** (R^{tot}=0.445) DEER-docked complex from the set of PatchDock/FireDock complexes. Experimental traces are in black, with simulations in red/green. The pump to detection frequency offsets Δν are −65, 80, 165, 247, 330 MHz, for mutant 226-54 (NO•-NO•) Δν = 65 MHz. All traces have had the background $B(t)$ and the un-modulated part (1-Δ) removed and then $\Delta f(t)$ is plotted (see Eq. 2). Note that some DEER traces exhibit weak oscillations from ^{14}N and ^{1}H electron-nuclear interactions, see Figure S4 for further details.

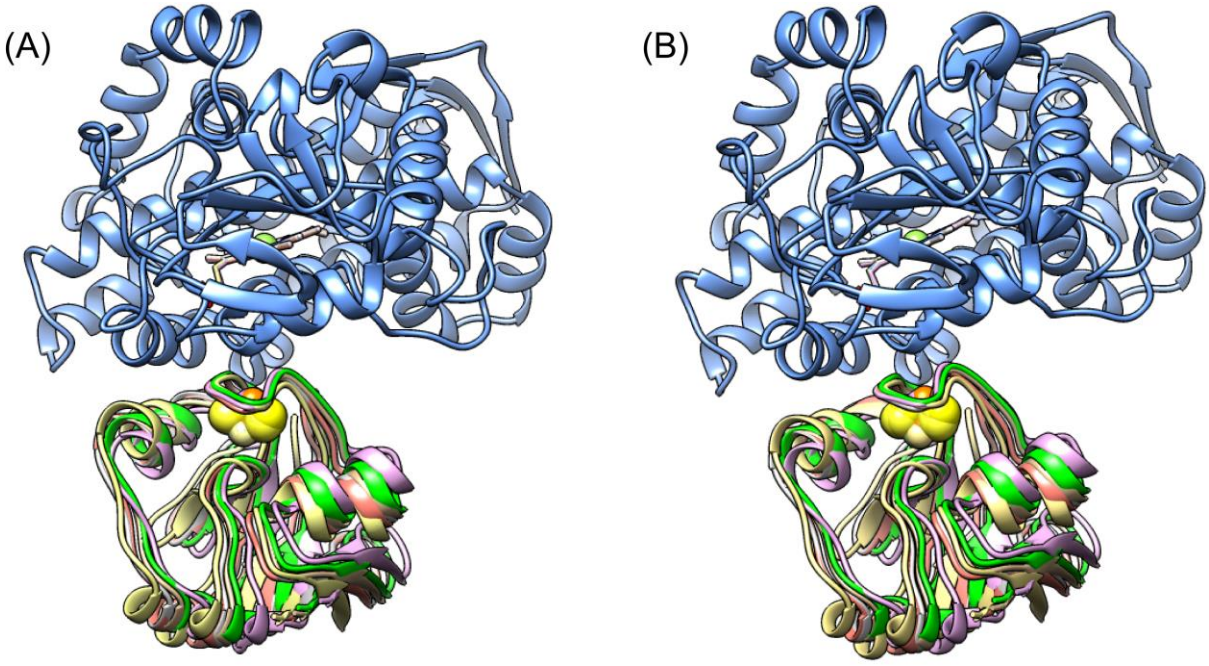

Fig. S10. Overlay of the structures of the top six best-ranked DEER-docked complexes after geometry optimization (A) in water and (B) in vacuum, using the MD program Gromacs. The CYP199A2 component of each complex is structurally aligned to that of the top-ranked structure to show the orientation of HaPux on the CYP199A2 proximal surface, CYP1099A2 is colored blue with the Heme Fe colored mint green. HaPux is colored green (with orange Fe in the Fe-S cluster) for Rank1, tan with matching Fe for Rank2, lilac for Rank3, cream for Rank4, peach for Rank5, and grey for Rank6. As can be seen from the comparison of (A) and (B); the results of the two geometry optimizations are very similar.

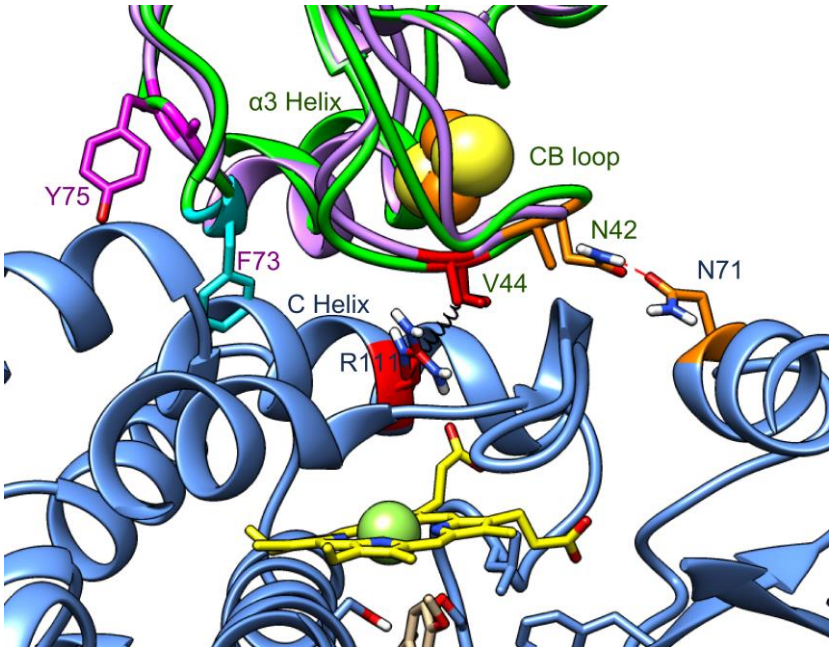

Fig. S11. Superposition of the structure of PuxB (purple, PDB code: 3HUI), a [Fe_2S_2] ferredoxin from *Rhodopseudomonas palustris* CGA009 that shows slow but detectable electron transfer to CYP199A2, onto the structure of HaPux (green) in the DEER-docked derived model of the CYP199A2-HaPux complex.[13] The side chain clash of Phe73 of PuxB, a Gly in HaPux, shown in cyan with the C helix of CYP199A2 (blue), and the potential clash of Tyr75, Ala in HaPux, shown in magenta with the D helix are evident. The favorable hydrophobic interaction between Val44 in HaPux and Arg111 in CYP199A2 (shown as a black spring between red residues) is changed in PuxB as Val44 is replaced by Ala. Finally, the absence of the hydrogen bond between Asn42 of HaPux (Ala42 in PuxB) and Asn71 of CYP199A2, residues shown in orange, is also important.

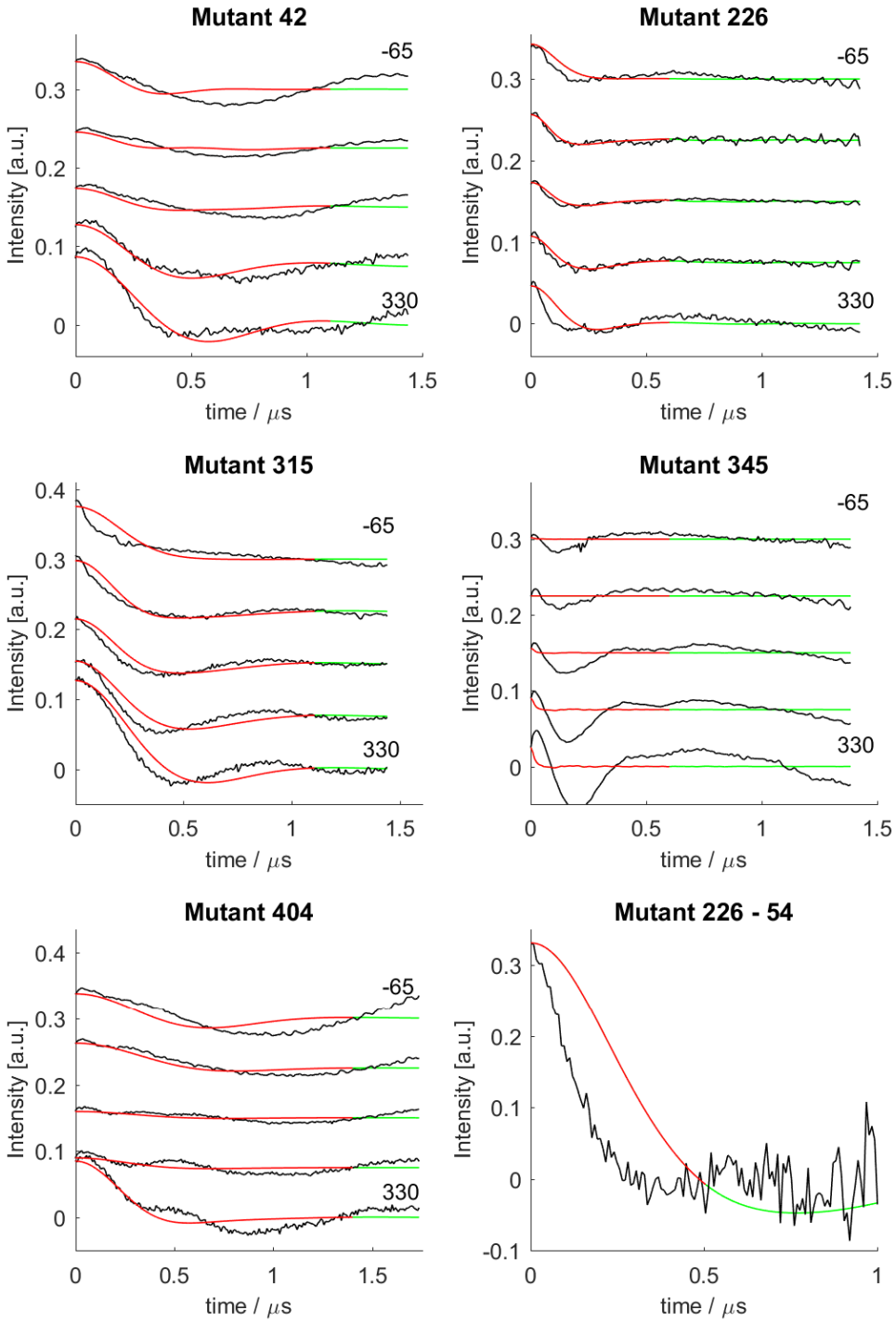

Fig. S12. DEER simulation using a complex where CYP199A2 and HaPux are aligned to the crystal structure of the P450cam-putidaredoxin (P450cam-Pdx) complex from *Pseudomonas putida*.[14] The simulations show a poor match to the experiment data with R^{tot} = 0.1101. The P450cam-Pdx structure has Pdx rotated about 90 degrees counter-clockwise about the heme(Fe)-Fe1 axis (viewed from the heme to the Fe-S cluster) as compared to the best DEER docked CYP199A2-HaPux complex. In this model of the complex the mean Fe-S to NO• distances are (values in the bracket are from the best ranked DEER-docked complex): Mutant 42: 37 (40) Å, Mutant 226: 27 (23) Å, Mutant 315: 36 (35) Å, Mutant 345: 17 (26) Å, Mutant 404: 40 (43) Å, Mutant 54-226: 39 (31) Å. Since the distance between the redox centers is similar, the NO-to-Fe-S mean DEER distances of the aligned P450cam-Pdx complex are similar to the best ranked DEER-docked complex, and the poor match of the simulations to the experimental data is due to the orientation. The DEER trace for the NO•-NO• mutant 226-54 indicates a mean distance of 30 Å, whereas the aligned P450cam-Pdx complex has a significantly longer distance of 40 Å.

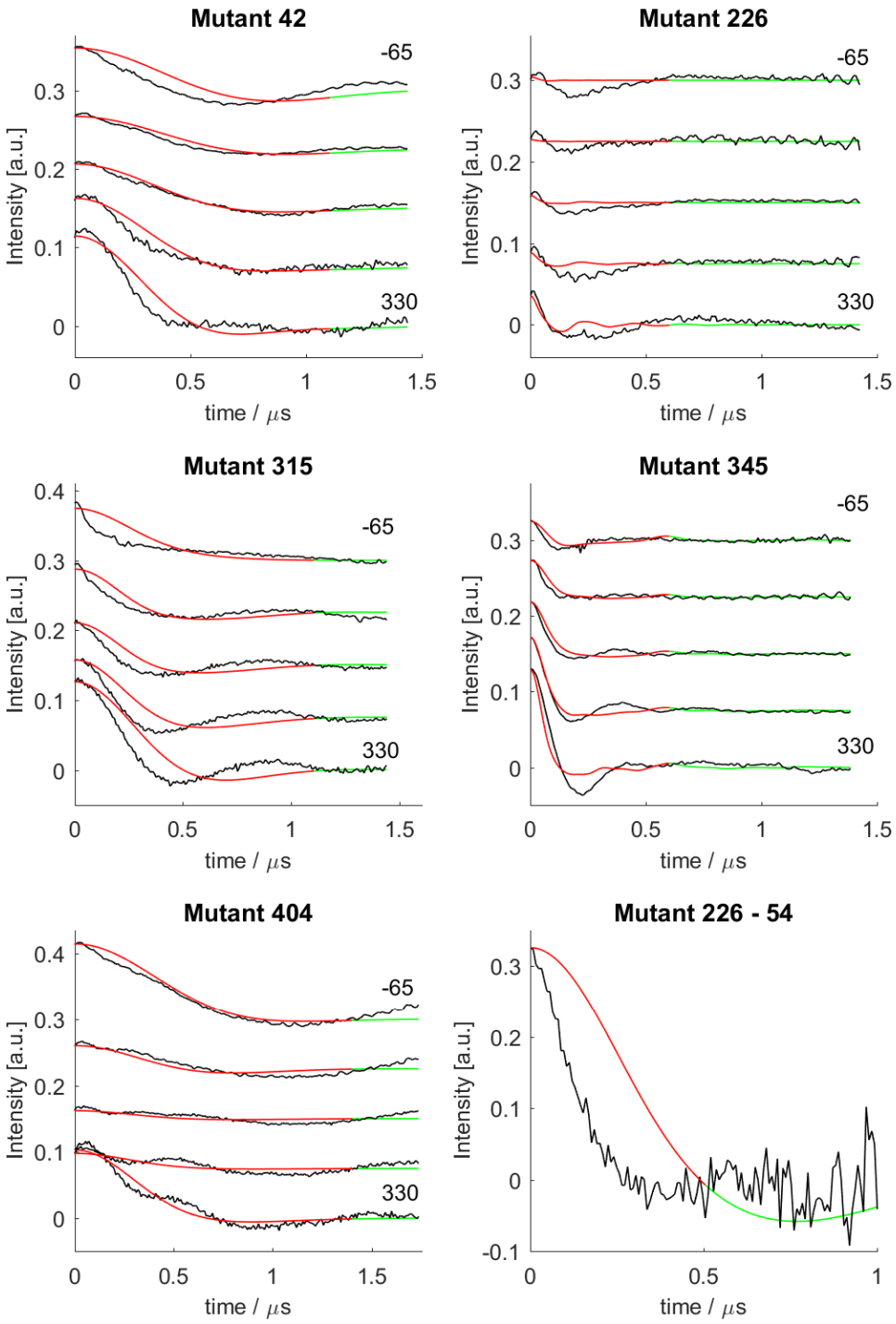

Fig. S13. DEER simulation using a complex where CYP199A2 and HaPux are aligned to the crystal structure of the CYP11A1-adrenodoxin (CYP11A1-Adx) complex from mitochondria.[15] The simulations show a poor match to the experiment data with R^{tot} = 0.1138. The CYP11A1-Adx structure has Adx rotated about 150° degrees counter-clockwise about the Heme(Fe)-Fe1 axis (viewed from the heme towards the Fe-S cluster) as compared to the best ranked DEER-docked CYP199A2-HaPux complex. In this model of the complex the mean Fe-S to NO• distances are (values in the bracket are from the best ranked DEER-docked complex): Mutant 42: 42 (40) Å, Mutant 226: 20 (23) Å, Mutant 315: 38 (35) Å, Mutant 345: 26 (26) Å, Mutant 404: 43 (43) Å, Mutant 54-226: 39 (31) Å. Since the distance between the redox centers is similar, the NO-to-Fe-S mean DEER distances of the aligned CYP11A1-Adx complex are similar to the best ranked DEER-docked complex, and the poor match of the simulations to the experimental data is due to the orientation. The DEER trace for the NO•-NO• mutant 226-54 indicates a mean distance of 30 Å, whereas the aligned CYP11A1-Adx complex has a significantly longer distance of 41 Å.

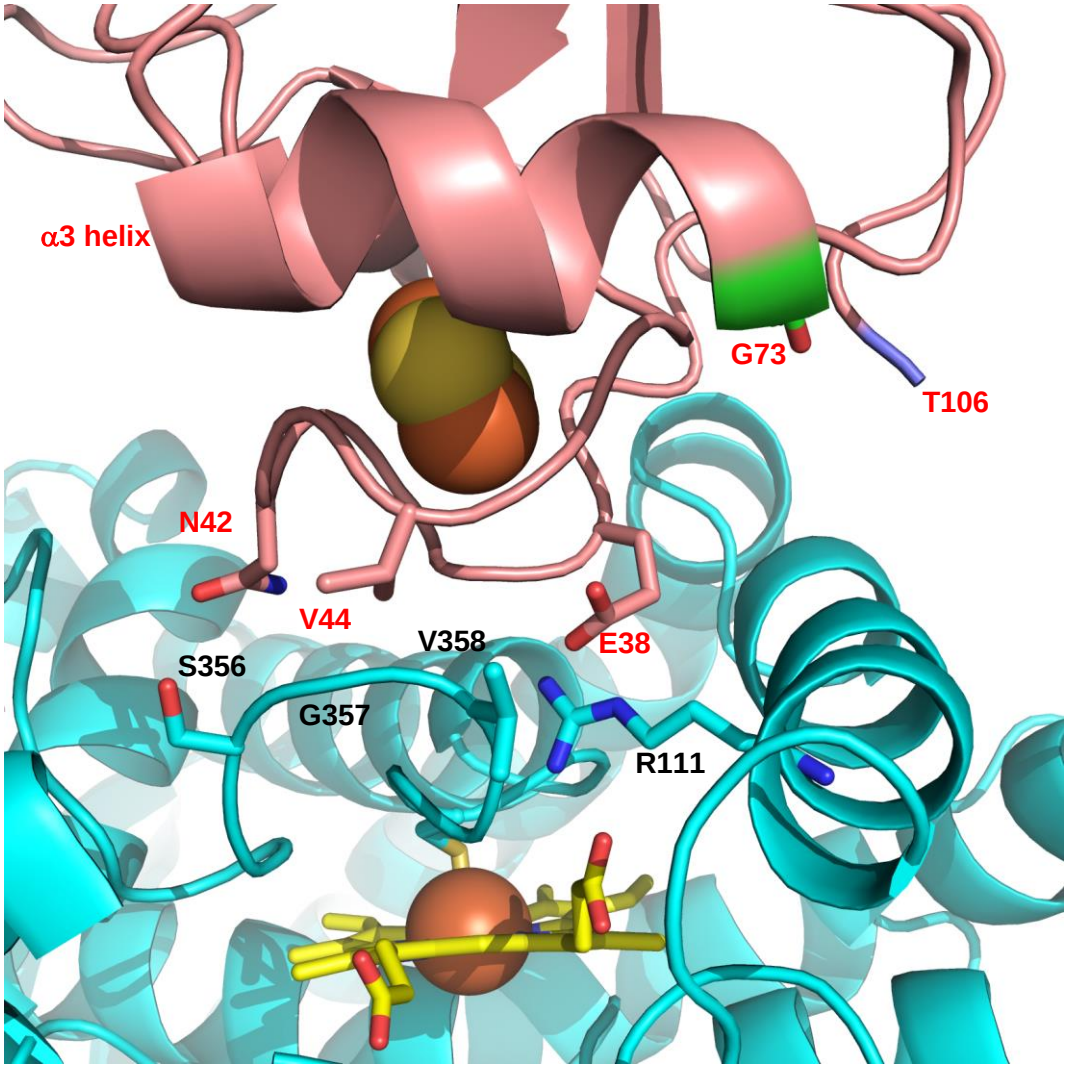

Fig. S14. The interfacial contacts between CYP199A2 (cyan, heme in yellow, residue numbers in black) and HaPux (salmon, residue numbers in red) after structural alignment to P450cam and Pdx, respectively, in the crystal structure of the P450cam-Pdx complex from *Pseudomonas putida*.[14] Side chain clashes were relieved by performing an energy minimisation in UCSF Chimera using the minimise structure functionality.[16-20] Within the cluster-binding loop E38 of HaPux is H-bonded to R111, V44 contacts G357, and N42 forms a H-bond with S356. The α3 helix and the C-terminus residue (T106, in blue) of HaPux do not make contact with CYP199A2 residues. The lower number of residue contacts is expected to weaken CYP199A2-HaPux binding compared to the more complementary contacts in the model structure derived from DEER constraints. Notably, G73 (green) of HaPux is exposed to the solvent which is not consistent with the highly beneficial effect of the F73G mutation of PuxB for CYP199A2 binding, nor does the structure indicate why the A42N and A44V mutations in PuxB should increase the rate of electron transfer without improving PuxB-CYP199A2 binding.

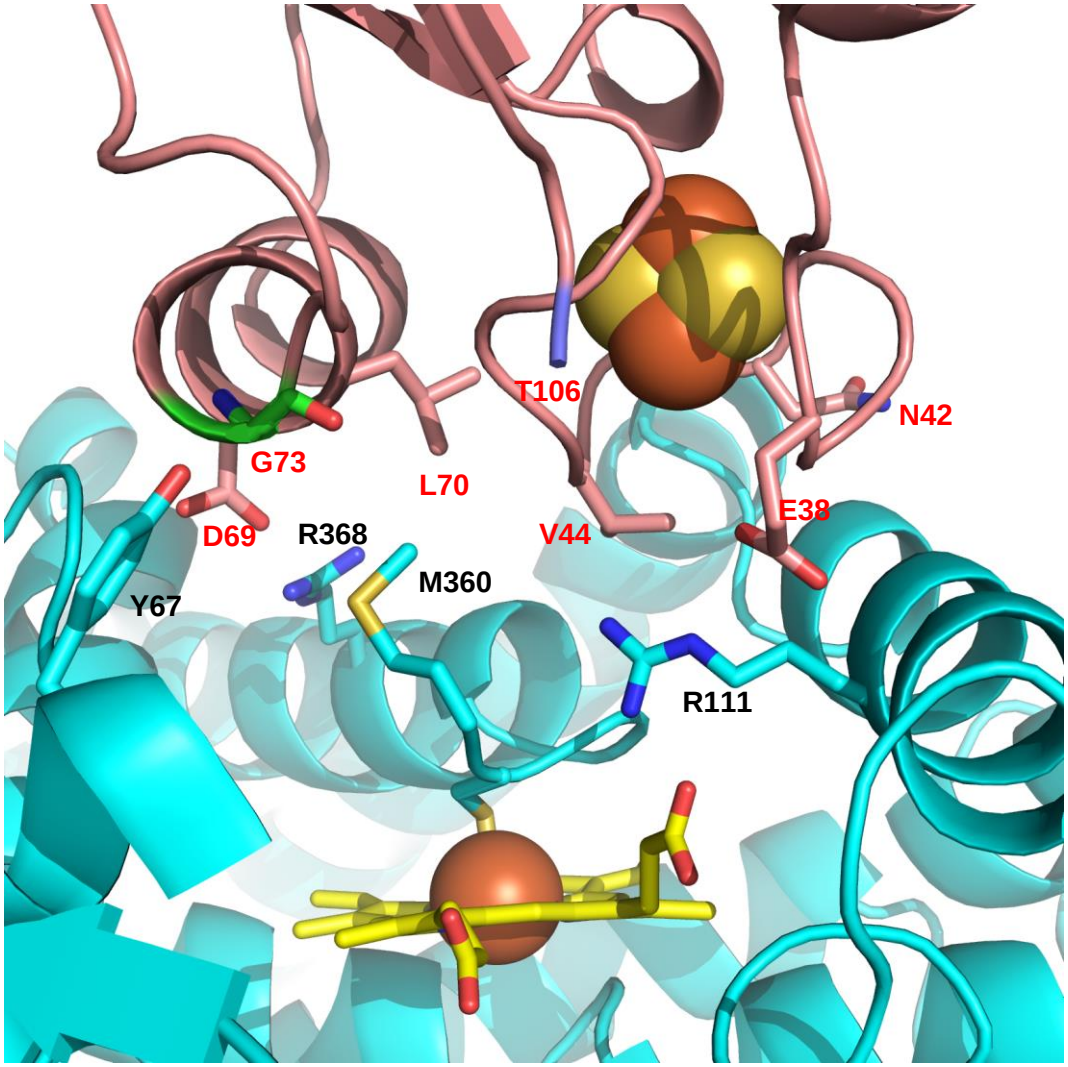

Fig. S15. The interfacial contacts between CYP199A2 (cyan, heme in yellow, residue numbers in black) and HaPux (salmon, residue numbers in red) after structural alignment to CYP11A1 and Adx, respectively, in the crystal structure of the CYP11A1-Adx complex from mitochondria.[15] Side chain clashes were relieved by performing an energy minimisation in UCSF Chimera using the minimise structure functionality. [16-20] The HaPux E38 is directed into a hydrophobic patch and too far away to interact with R111 while in the DEER-derived structure it forms a salt bridge with R111. N42 is solvent-exposed and does not interact with CYP199A2 residues. V44 contacts R111 but there are fewer contacts compared to the DEER-derived structure. D69 in the HaPux α3 helix forms a salt bridge with R368 of CYP199A2 while L70 contacts M360. The C-terminus T106 (blue) does not contact CYP199A2. Interestingly, however, G73 (green) of HaPux is close to Y67 of CYP199A2, which is consistent with the effect of the F73G mutation promoting binding of PuxB to CYP199A2. Overall, this structure is plausible for a CYP199A2-HaPux complex although there are fewer interfacial contacts than in the DEER-derived structure, suggesting weaker binding.

References

(1) Bell, S. G.; Hoskins, N.; Xu, F.; Caprotti, D.; Rao, Z.; Wong, L. L. *Biochem. Biophys. Res. Commun.* **2006**, *342*, 191.
(2) Bell, S. G.; Tan, A. B.; Johnson, E. O.; Wong, L. L. *Mol. Biosyst.* **2010**, *6*, 206.
(3) Bell, S. G.; Xu, F.; Forward, I.; Bartlam, M.; Rao, Z.; Wong, L. L. *J. Mol. Biol.* **2008**, *383*, 561.
(4) Xu, F.; Bell, S. G.; Peng, Y.; Johnson, E. O.; Bartlam, M.; Rao, Z.; Wong, L. L. *Proteins Struct. Funct. Bioinf.* **2009**, *77*, 867.
(5) Bell, S. G.; Yang, W.; Tan, A. B.; Zhou, R.; Johnson, E. O.; Zhang, A.; Zhou, W.; Rao, Z.; Wong, L. L. *Dalton Trans.* **2012**, *41*, 8703.
(6) Omura, T.; Sato, R. *J. Biol. Chem.* **1962**, *237*, 1375.
(7) Otwinowski, Z.; Minor, W. *Methods Enzymol.* **1997**, *276*, 307.
(8) McCoy, A. J.; Grosse-Kunstleve, R. W.; Adams, P. D.; Winn, M. D.; Storoni, L. C.; Read, R. J. *J. Appl. Crystallogr.* **2007**, *40*, 658.
(9) Smith, N.; Mayhew, M.; Holden, M. J.; Kelly, H.; Robinson, H.; Heroux, A.; Vilker, V. L.; Gallagher, D. T. *Acta Crystallogr. D: Biol. Crystallogr.* **2004**, *60*, 816.
(10) Emsley, P.; Cowtan, K. *Acta Crystallogr. D: Biol. Crystallogr.* **2004**, *60*, 2126.
(11) Murshudov, G. N.; Skubak, P.; Lebedev, A. A.; Pannu, N. S.; Steiner, R. A.; Nicholls, R. A.; Winn, M. D.; Long, F.; Vagin, A. A. *Acta Crystallogr. D: Biol. Crystallogr.* **2011**, *67*, 355.
(12) Chen, V. B.; Arendall, W. B., 3rd; Headd, J. J.; Keedy, D. A.; Immormino, R. M.; Kapral, G. J.; Murray, L. W.; Richardson, J. S.; Richardson, D. C. *Acta Crystallogr. D: Biol. Crystallogr.* **2010**, *66*, 12.
(13) Andralojc, W.; Hiruma, Y.; Liu, W. M.; Ravera, E.; Nojiri, M.; Parigi, G.; Luchinat, C.; Ubbink, M. *Proc. Natl. Acad. Sci. U.S.A.* **2017**, *114*, E1840.
(14) Tripathi, S.; Li, H.; Poulos, T. L. *Science* **2013**, *340*, 1227.
(15) Strushkevich, N.; MacKenzie, F.; Cherkesova, T.; Grabovec, I.; Usanov, S.; Park, H.-W. *Proc. Natl. Acad. Sci. U.S.A* **2011**, *108*, 10139.
(16) Wang, J. M.; Wang, W.; Kollman, P. A.; Case, D. A. *J. Mol. Graph. Model.* **2006**, *25*, 247.
(17) Widge, A. S.; Matsuoka, Y.; Kurnikova, M. *J. Mol. Graph. Model.* **2008**, *27*, 34.
(18) Hinsen, K. *J. Comput. Chem.* **2000**, *21*, 79.
(19) D.A. Case; D.S. Cerutti; T.E. Cheatham, I.; Darden, T. A.; Duke, R. E.; Giese, T. J.; Gohlke, H.; Goetz, A. W.; Greene, D.; Homeyer, N.; Izadi, S.; Kovalenko, A.; Lee, T. S.; LeGrand, S.; Li, P.; Lin, C.; Liu, J.; Luchko, T.; Luo, R.; Mermelstein, D.; Merz, K. M.; Monard, G.; Nguyen, H.; Omelyan, I.; Onufriev, A.; Pan, F.; Qi, R.; Roe, D. R.; Roitberg, A.; Sagui, C.; Simmerling, C. L.; Botello-Smith, W. M.; Swails, J.; Walker, R. C.; Wang, J.; Wolf, R. M.; Wu, X.; Xiao, L.; York, D. M.; Kollman, P. A. *AMBER 2017, University of California, San Francisco* **2017**.
(20) Pettersen, E. F.; Goddard, T. D.; Huang, C. C.; Couch, G. S.; Greenblatt, D. M.; Meng, E. C.; Ferrin, T. E. *J. Comput. Chem.* **2004**, *25*, 1605.